Photoionization microscopy of the lithium atom: Wave-function imaging of quasibound and continuum Stark states

S. Cohen,[1] M. M. Harb,[2] A. Ollagnier,[2] F. Robicheaux,[3] M. J. J. Vrakking,[4] T. Barillot,[2] F. Lépine,[2] and C. Bordas[2]

[1]*Atomic and Molecular Physics Laboratory, Physics Department, University of Ioannina, 45110 Ioannina, Greece*
[2]*Institut Lumière Matière, Université Lyon 1, CNRS, UMR5306, 10 Rue Ada Byron, 69622 Villeurbanne Cedex, France*
[3]*Department of Physics and Astronomy, Purdue University, West Lafayette, Indiana 47907, USA*
[4]*Max-Born-Institut, Max Born Straße 2A, D-12489 Berlin, Germany*

Photoionization of an atom in the presence of a uniform static electric field provides the unique opportunity to expand and visualize the atomic wave function at a macroscopic scale. In a number of seminal publications dating back to the 1980s, Fabrikant, Demkov, Kondratovich, and Ostrovsky showed that this goal could be achieved by projecting slow (meV) photoionized electrons onto a position-sensitive detector and underlined the distinction between continuum and resonant contributions. The uncovering of resonant signatures was achieved fairly recently in experiments on the nonhydrogenic lithium atoms [Cohen *et al.*, Phys. Rev. Lett. **110**, 183001 (2013)]. The purpose of the present article is the general description of these findings, with emphasis on the various manifestations of resonant character. From this point of view, lithium has been chosen as an illustrative example between the two limiting cases of hydrogen, where resonance effects are more easily identified, and heavy atoms like xenon, where resonant effects were not observed.

I. INTRODUCTION

Our intimate knowledge of atomic-scale systems and their quantum description is entirely based on the key concept of the wave function, obtained by solving the Schrödinger equation. Nevertheless, and with very few exceptions, the wave function, or its squared modulus, is generally not measured directly. Great progress has been achieved in recent years towards the development of a variety of strategies and approaches, aiming to a more-or-less direct and, if possible, complete observation of the wave function itself. These approaches depend, of course, on the intrinsic nature of the system under study. For example, microscopy techniques, such as scanning tunneling or atomic force microscopy, were employed for the detection of photoemission from a molecule deposited on a surface [1,2] and allowed for the reconstruction of its molecular orbitals [3]. Furthermore, imaging methods in conjunction with strong laser fields permitted the tomographic reconstruction of the electron density of ground-state atoms and small molecules [4,5]. On the other hand, the development of quantum optics in connection with weak-measurement concepts [6] and experiments [7] led to the complete (amplitude and phase) determination of the wave function of the photon [8]. In the present article we exploit another imaging technique, so-called photoionization microscopy, suitable for the experimental observation of the squared modulus of the wave function of an electron emitted from an atomic system. This is achieved by recording the two-dimensional flux of very slow electrons ejected in an ionization process in the presence of a static electric field. At present the method cannot provide information on the wave function's phase. Nevertheless, it is one out of a few, if not the only one, having the advantage that the squared modulus of the wave function is *directly* recorded, i.e., it is projected and it is visible on the surface of the detector without any requirements for further processing, hypotheses, or tomographic inversion.

Within the context discussed here, the term "microscopy" refers to the experimental capability of extending the atomic or molecular wave function to macroscopic dimensions. From this point of view, the photoionization of a simple atom in the presence of an external electric field constitutes a perfect case study, owing to the coexistence of purely continuum as well as quasibound atomic states (resonances) just above the ionization threshold. In that sense, photoionization microscopy does not provide access solely to free-electron wave functions, but provides access also to atomic wave functions of quasibound states, the latter bearing intrinsic properties of the atomic system under study. The above notions were explored for the first time during the 1980s and early 1990s by Fabrikant, Demkov, Kondratovich, and Ostrovsky in a famous series of articles devoted to a thorough and essentially semiclassical analysis of the hydrogenic Stark effect [9–12]. Dealing first with the simpler case of photodetachment [10], the connection between interference patterns and classical electron trajectories was then extended to the far more complicated case of photoionization. In that latter case, the presence of narrow Stark resonances and their impact on the interference patterns was examined separately.

A photodetachment microscope [13] was experimentally implemented soon after the emergence of photoelectron imaging techniques [14]. This experimental breakthrough verified unambiguously the close connection between quantum interferences and classical trajectories, allowing in addition for electron affinity measurements with unprecedented accuracy [15]. A few years later photoionization microscopy experiments were performed with xenon atoms [16–18]. Remarkably, in all these experiments, the number and position of nodes of the recorded wave function evolved smoothly with photon energy, and remained to a large extent insensitive to the presence of resonances. This fact was attributed to the coupling between continuum and quasibound states, induced by the large ionic Xe^+ core. This interaction is absent in the hydrogen atom because of the orthogonality between its continuum and quasibound states. Nevertheless, subsequent [19] as well as recent [20–22] theoretical developments predicted that the

observation of resonant effects in nonhydrogenic atoms is indeed also possible under certain conditions. It became, however, evident that a first step towards this goal is the observation of resonant phenomena in atoms with a single valence electron outside closed (sub)shells, the latter forming an ionic core of small size in order to minimize the aforementioned coupling. We have indeed demonstrated recently the appearance of resonant signatures in photoionization of lithium atoms [23], immediately followed by a clear demonstration in the hydrogen atom itself [24]. This latter experiment fully verified old, as well as recent [25,26], theoretical works. Finally, another experimental demonstration of resonant effects was even more recently achieved in helium atoms [27].

The purpose of the present article is a detailed description of our findings in the lithium experiment over the whole energy range between the saddle-point energy and the zero-field ionization limit. The small ionic core of this atom allows for the observation of resonant effects. Lithium is therefore representative of a general atomic system standing between hydrogen (exhibiting clear resonant effects) and heavy atoms like xenon (where no resonant effects were experimentally observed). Emphasis will be given to the differences observed between the continuum and the resonant images of wave functions, as well as their connection with the aforementioned recent experimental achievements [24,27] and theoretical work [19–22]. A quite brief presentation of our nonresonant data was given in [28], for the purpose of testing the so-called coupled-channel theory. Here, however, the interpretation of our experimental results is based on an electron wave-packet propagation approach, relying on solving the time-dependent Schrödinger equation (TDSE).

The rest of the article is organized as follows: In the second section we describe the photoionization microscope as well as the full experimental setup and procedure. Next, we briefly review the essential points of the theory of the Stark effect [11,12,29] upon which photoionization microscopy is based, as well as the computational, TDSE-solving, procedure providing radial distributions that can be compared with the experimental ones. The fourth section is devoted to a presentation and discussion of both our continuum and resonant experimental results on lithium. Finally, in the concluding section, we discuss perspectives for further work.

II. EXPERIMENTAL SETUP AND PROCEDURE

In our experiment a beam of lithium atoms is produced by laser ablation of a pure lithium metallic rod. The lithium atoms are entrained in a pulsed helium gas jet controlled by a piezoelectric valve operated at 10 Hz. The source chamber is pumped by a 750 l/s diffusion pump. The lithium beam enters the interaction chamber through a 1-mm-diameter skimmer placed 2 cm downstream from the nozzle. The interaction chamber is pumped by a 250 l/s turbomolecular pump. The beam of ground-state lithium atoms interacts at right angles with a tunable UV laser beam delivered by a high-finesse optical parametric oscillator system (Spectra-Physics MOPO). The system operates at a repetition rate of 10 Hz and delivers light pulses of $\sim$1 mJ energy and $\sim$5 ns duration. Its $\sim$0.05 cm^{-1} linewidth is adequate for resolving Stark spectral structures that may be separated by less than 1 cm^{-1} and

for avoiding any blurring of the image interference patterns. The atomic and laser beams are both perpendicular to the electron spectrometer (and electric field) axis. The final Stark states are single-photon excited out of the $^2S_{1/2}$ ($1s^2 2s$) lithium ground state (wavelength range 232–228 nm) and their azimuthal quantum number m is selected by directing the linear laser polarization either along the direction of the electric field (dipole selection rule $\Delta m = 0$), or perpendicular to it ($|\Delta m| = 1$).

Our microscope is similar to the one employed in earlier experiments [16–18,30]. It is based on a standard three-electrode velocity-map imaging (VMI) spectrometer design [31], and a full analytical description of its geometry, dimensions, and operating conditions is available in [32]. Photoionization takes place in the center between the first two electrodes: a solid repeller plate and an extractor plate with a hole in its center. These electrodes are biased at voltages V_R and V_E respectively. The third electrode is grounded and of the same design as the extractor plate. The holes of the last two electrodes create an inhomogeneous electric field allowing the fulfillment of the VMI condition [31]. The field variation near the center of the interaction region is roughly linear. It amounts to about 2%/mm along the spectrometer axis and about 0.1%/mm transversely to this axis [32]. For maintaining an overall electric field variation below $\pm$0.1%, we limit the axial dimension of the interaction volume below 200 μm (by moderately focusing the laser beam using an $\approx$25-cm–focal-length lens) and its transverse dimension below 2 mm (by placing a diaphragm transversely to the lithium beam path at the entrance of the spectrometer). Hence, within the limited laser-atom interaction volume the field may be considered as being nearly constant.

Photoelectrons resulting from the photoionization of lithium atoms are accelerated by the field towards the end of a field-free drift tube. An electrostatic magnifying Einzel lens, consisting of three identical equally spaced electrodes with holes at their centers, is placed in the middle of this tube [33]. A voltage V_L is applied to the middle electrode, while the other two are grounded. The electrons are detected at the end of the drift region by a two-dimensional position-sensitive detector (PSD). The PSD is made of a tandem microchannel plate (MCP) assembly followed by a phosphor screen. A CCD camera is used to record the two-dimensional distribution of the light spots on the phosphor screen. Recorded images are transferred to a PC, where they are accumulated over several thousand laser shots. In order to improve the signal-to-noise ratio the MCP is operated with a 100-ns gate [34]. The entire spectrometer, including the electrodes, the drift tube, and the detector assembly, is shielded against external magnetic fields by a double μ-metal layer, ensuring a magnetic field below 1 μT in its interior.

The VMI condition [31] is fulfilled for a given ratio of the voltages V_R and V_E, which is determined by the design of the spectrometer and moderately depends on whether the Einzel lens is on or off. The chosen values of V_R, V_E, and V_L result in a field strength $F \approx 1$ kV/cm at the center of the interaction region and an up to $\sim$20-fold magnification of the images. For $\sim$10 meV electrons (roughly the range of interest in our experiments) such a magnification leads to typical image sizes of $\sim$10 mm and a $\sim$1 mm spacing between consecutive

fringes. Without any magnification the same images would have a size of ~ 1 mm and a fringe separation of $\sim 100 \, \mu$m. This separation is comparable to the resolution limit of our PSD and would make the observation of the structure of the wave function hardly achievable.

III. PRINCIPLES OF PHOTOIONIZATION MICROSCOPY AND THEORETICAL CALCULATIONS

A. Qualitative quantum mechanical description

Let us begin by presenting the principles of photoionization microscopy by means of a review of the quantum mechanical theory of the Stark effect. The Hamiltonian of a hydrogen atom ($Z = 1$) in a uniform static electric field of strength F directed along the z axis [Fig. 1(a)], is separable in parabolic coordinates $\xi = r + z$, $\eta = r - z$, and $\varphi = \arctan(y/x)$. Separability along φ leads to the azimuthal quantum number m, while separability along ξ and η involves two separation constants, Z_1 and $Z_2 = Z - Z_1$, and leads to parabolic quantum numbers n_1 and n_2, counting the nodes in the ξ and η parts of the wave function, respectively [11,12,29,35]. Due to the asymptotic form of the ξ potential curve $V_1(\xi)$ for $\xi \to \infty$, the electron motion is always bound along the ξ coordinate [see Fig. 1(c)]. The energy range of interest here is located between the classical saddle-point energy $E_{sp}^{cl} = -2F^{1/2}$ atomic units (a.u.) and the field-free ionization limit $E = 0$. For $E \geqslant E_{sp}^{cl}$ the asymptotic behavior of the η-potential curve $V_2(\eta)$ for $\eta \to \infty$ allows the escape of the electron in the negative z direction, along the η coordinate [Figs. 1(d) and 1(e)].
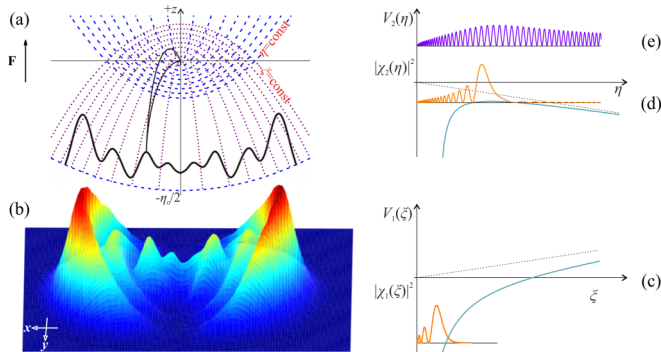

FIG. 1. Wave-function microscopy aims at observing the spatial structure of the electronic wave function. (a) The electron flux stemming from the photoionization of an atom in the presence of a static electric field is recorded perpendicularly to the field and at macroscopic distance, i.e., approximately along a given constant $\eta = \eta_o$ paraboloid. (b),(c) The image corresponds to the squared modulus of the wave function along the ξ coordinate where the electron motion is always bound. In (b) the nodes of the wave function are clearly observed in the example shown (with x and y denoting the detector plane), recorded with $F \approx 1 \, \text{kV/cm}$ and electron excitation energy exceeding E_{sp}^{cl} by 10 meV. Depending on the electron energy with respect to the maximum of the η potential, the classical electron motion may be either bound (d) or free (e). In the former case the electron can escape solely via tunneling and the image corresponds to a direct macroscopic projection of a quantum standing wave characterizing the quasibound electronic state (n_1^{res}, n_2^{res}, m) where the electron is initially localized within the inner η-potential well.

Each n_1 is associated with a threshold $E_{thr}^{n_1}$, found by solving the equation $E = -2[Z_2(E,m,F,n_1)F]^{1/2}$ [29]. For a given n_1 the quantum number n_2 is meaningful only when $E < E_{thr}^{n_1}$. Each (n_1, n_2) pair corresponds to a quasibound state for which the electron escapes solely via *tunneling* through the η potential [Fig. 1(d)]. For $E > E_{thr}^{n_1}$ where n_2 loses its meaning, the electron escapes *over* the η-potential barrier [Fig. 1(e)]. Thus, within $E_{sp}^{cl} \leqslant E \leqslant 0$ quasidiscrete and continuum Stark states with different n_1 values coexist. All hydrogenic Stark states with different n_1 are orthogonal to each other.

Wave-function microscopy aims at recording the photocurrent density,

$$j(\xi, \eta) \propto i\left[\psi \frac{\partial \psi^*}{\partial \eta} - \psi^* \frac{\partial \psi}{\partial \eta}\right] \quad (1)$$

at a macroscopic distance, along a given constant $\eta = \eta_o$ paraboloid which crosses the z axis at $z = z_o = -\eta_o/2$ where the detector is located [see Figs. 1(a) and 1(b)] [16,18]. In Eq. (1) ψ is the final-state electron wave function. Since $\eta_o \to \infty$ while the ξ motion is bound, it holds that $\xi \ll \eta_o$ and the paraboloid may be well approximated by a plane perpendicular to the z axis. It is to be emphasized that, although wave-function microscopy experiments provide directly photoelectron angular distributions [36], the aforementioned interference patterns refer principally to the radial distributions of the observed images.

Let us consider first the continuum spectrum in the absence of any resonance and denote by n_1^o the highest quantum number corresponding to an open n_1 channel for a given E (i.e., $E_{thr}^{n_1^o} \leqslant E \leqslant E_{thr}^{n_1^o+1}$). Then, Eq. (1) for this so-called background (BG) density is put into the form

$$j_{BG}(\xi, \eta = \eta_o) \propto \left| \sum_{n_1=0}^{n_1^o} c_{n_1} \chi_{1,n_1}(\xi) \right|^2, \quad (2)$$

where χ_{1,n_1} denotes wave functions along the ξ coordinate and c_{n_1} the corresponding weights which depend on the excitation process. The coherent superposition of Eq. (2) has the form of an interferogram, which is dominated by χ_{1,n_1^o} and exhibits n_1^o dark fringes. As is made evident from Fig. 2, n_1^o increases monotonically with energy for a given field strength.

Let us now consider the additional presence of a single narrow resonance corresponding to a quasibound state and associated with a parabolic quantum number n_1^{res}. Given that $E < E_{thr}^{n_1^{res}}$ and $E_{thr}^{n_1^o} \leqslant E \leqslant E_{thr}^{n_1^o+1}$, it necessarily holds that $n_1^{res} > n_1^o$. The quasidiscrete state's wave function $\chi_{1,n_1^{res}}(\xi)$ modifies the photocurrent density $j(\xi, \eta = \eta_o)$ according to

$$j_{BG+res}(\xi, \eta = \eta_o) \propto \left| a_{n_1^{res},n_2} \chi_{1,n_1^{res}}(\xi) + \sum_{n_1=0}^{n_1^o} c_{n_1} \chi_{1,n_1}(\xi) \right|^2, \quad (3)$$

where the weight $a_{n_1^{res},n_2}$ depends on n_2. The latter, however, cannot, in principle, be extracted from $j_{BG+res}(\xi, \eta = \eta_o)$. For a sufficiently narrow resonance, the wave function $\chi_{1,n_1^{res}}$ dominates the interferogram. Therefore, $j_{BG+res}(\xi, \eta = \eta_o)$ is expected to evolve nonmonotonically in the vicinity of resonances. Specifically, quantitative calculations [12,25] reveal the following on-resonance characteristics:
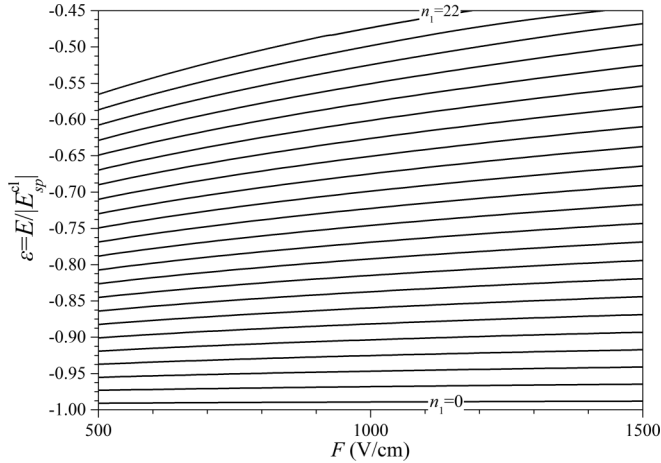
FIG. 2. Parabolic n_1-channel threshold energies $E_{\text{thr}}^{n_1}$ as a function of the strength of the static electric field, for $Z = 1$, $m = 0$, and quantum numbers $n_1 = 0-22$. The thresholds are given in terms of the dimensionless energy parameter $\varepsilon = E/|E_{sp}^{\text{cl}}|$, where the classical saddle-point energy (corresponding to $\varepsilon = -1$) is $E_{sp}^{\text{cl}} = -2F^{1/2}$ a.u. $\approx -6.121[F(\text{V/cm})]^{1/2}$ cm^{-1}. The thresholds were determined by solving the equation $E = -2[Z_2(E,F,m,n_1)F]^{1/2}$, where the separation constants $Z_2(E,F,m,n_1) = Z-Z_1(E,F,m,n_1)$ were computed by solving the Coulomb-Stark Schrödinger equation along the ξ coordinate.

(i) A strong modification of the interference pattern that can include a fringe number change. Hence, $j_{\text{BG+res}}(\xi,\eta = \eta_{\text{o}})$ can exhibit n_1^{res} dark fringes while their number is reduced to n_1^{o} at electron excitation energies just below and just above the resonance.

(ii) A modulation of the fringe contrast due to the coherent superposition of resonant and nonresonant contributions in Eq. (3).

(iii) A broadening of the image outer ring, associated with tunneling ionization. For the hydrogen atom, the effect was first pointed out by Kondratovich and Ostrovsky [12] (see Fig. 4 therein) and more thoroughly analyzed recently by Zhao and Delos [25]. It was also noticed by Texier in his Xe calculations [19]. It corresponds to an on-resonance increase of the tunneling probability through the potential barrier of $V_2(\eta)$ as a result of the electron's high localization near the edge of the potential.

The ultimate goal of photoionization microscopy is to uncover the features of $j(\xi,\eta = \eta_{\text{o}})$ stemming from the resonant state(s) $\chi_{1,n_1^{\text{res}}}$. For the hydrogen atom this was achieved quite recently [24]. Of course, the observation of these features in atoms more complex than hydrogen is of fundamental significance, as it will turn photoionization microscopy into a more general technique, eventually capable of dealing with polyatomic systems. However, the Hamiltonian of complex atoms in the presence of an external electric field is no longer separable in parabolic coordinates due to short-range interactions occurring when the excited electron penetrates the ionic core. This leads to a mixing between hydrogenic states of different n_1, which are no longer pure eigenstates of the atom. Hence, even if the system is initially prepared in a quasidiscrete state, it may "leak" (autoionize) to the degenerate continua. As a result the resonant features

(i)–(iii) may be obscured. The degree of core penetration can be assessed by a comparison of the magnitude of the quantum defects μ_ℓ for the ns, np, and nd Rydberg series. The substantial difference between xenon ($\mu_s \approx 4.0$, $\mu_p \approx 3.5$, and $\mu_d \approx 2.4$) and lithium ($\mu_s \approx 0.4$, $\mu_p \approx 0.05$, and $\mu_d \approx 0.002$) [37] quantum defects partly explains why resonant effects were not observed in the heavy xenon atom experiment [16,17] while being apparent in lithium [23]. The above arguments also suggest that the hydrogenic behavior can be induced by configuring the experiment in a manner where high-$|m|$ states are populated, suppressing contributions from highly penetrating low-ℓ orbitals. Moreover, it would be desirable to employ single-m excitation schemes in order to bypass the complications arising from interferences among different m components [19]. Finally, theoretical calculations demonstrating resonant effects in xenon [19] and the alkali-metal atoms [21] point towards an extreme sensitivity of the resonant manifestations to the field strength. This is compatible with the findings of the He experiment [27], where the resonant character was unveiled near avoided crossings [38] between pairs of resonances. Near the centers of these crossings, one of the resonances is decoupled from the degenerate continua, leaving tunneling as the only electron escape mechanism.

B. Connection between quantum mechanical and classical Coulomb-Stark problem

The classical treatment of the Coulomb-Stark problem deals solely with open n_1 channels, since tunneling is classically forbidden. Therefore, taking into account the above point (iii), it is expected that any deviations from the well-known classical energy dependence of the maximum radius of photoelectron impacts would potentially signal the presence of resonances. Our purpose here is to establish a connection between the classical and quantum mechanical descriptions of the problem, in order to unveil the conditions under which such deviations would be easier to observe.

Classical simulations [39] and subsequent experimental verifications [40,16,17] showed that a particular characteristic of slow photoelectron imaging is the appearance of two concentric structures in the recorded images. The outer one stems from classical source-to-detector electron trajectories, which are complicated and intersect the negative z axis at least once. The maximum classical radius $R_{\text{max}}^{\text{c}}$ of this so-called *indirect* contribution is related to the excitation energy through a simple analytical expression (see Eq. (11) of [39]). The inner structure (*direct* contribution) appears only for $E \geqslant E_{\text{dir}} \approx 0.775 E_{sp}^{\text{cl}}$ and stems from simple quasiparabolic trajectories that do not intersect the z axis. The classical radius R_{I} of the direct contribution is zero at $E = E_{\text{dir}}$ and its energy dependence is different from that of $R_{\text{max}}^{\text{c}}$ [39], but for $E > 0$ it approaches and finally matches $R_{\text{max}}^{\text{c}}$. A classification of the two contributions is provided via the electron's launch angle β with respect to the electric field. All escaping trajectories correspond to launch angles $\beta \geqslant \beta_c \equiv \arcsin[E/E_{sp}^{cl}](E \leqslant 0)$, while for $\beta < \beta_c$ the electron is classically bound. Note that $\beta_{\text{c}} = 0$ for $E \geqslant 0$. The indirect trajectories are distinguished from the direct ones through the angle β_{o} for which the corresponding trajectory intersects the z axis at infinity. Indirect trajectories correspond to launch
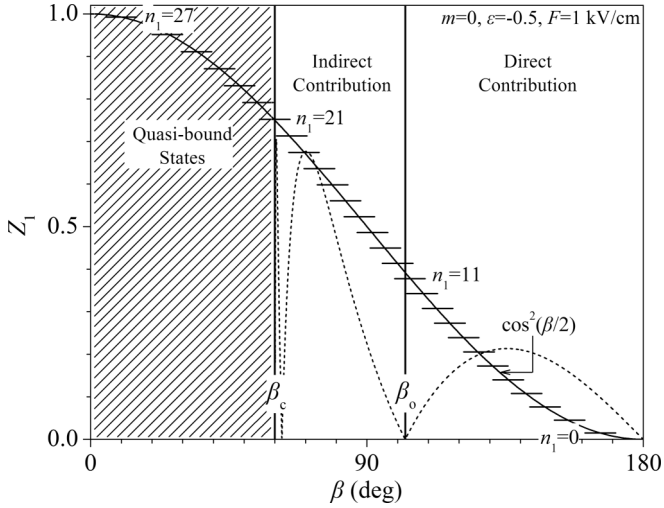
FIG. 3. Classical separation constant $Z_1 = Z\cos^2(\beta/2)$ (with $Z = 1$) (continuous line) as a function of the electron's launch angle β and the quantized quantum mechanical values $0 \leqslant Z_1^{n_1} \leqslant Z$ (drawn by horizontal line segments whose length is irrelevant), obtained by solving the Coulomb-Stark Schrödinger equation along the ξ coordinate for the ($\varepsilon = E/|E_{sp}^{cl}|$, F, m) set given in the plot. A few selected parabolic quantum numbers n_1 are provided next to the corresponding line segments. Also shown by vertical lines are the critical angles β_c and β_o, separating the regions related to quasibound states, indirect and direct contributions (see text), as well as the classical radius of impact on the detector (dashed line), computed as described in [39].

angles within the $[\beta_c, \beta_o]$ interval and the direct ones to the $[\beta_o, \pi]$ one.

A connection with the quantum description may be achieved through the separation constant Z_1, which is classically given by $Z_1 = Z\cos^2(\beta/2)$. On the other hand, the solution of the Schrödinger equation along the ξ coordinate provides a discrete set of separation constants $Z_1^{n_1} = Z_1(E, F, m, n_1)$. As an example, Fig. 3 shows the classical dependence of Z_1 as a function of β, along with the critical angles β_c and β_o and the computed quantum mechanical $Z_1^{n_1}$ values for $m = 0$, $F = 1$ kV/cm, and $\varepsilon \equiv E/|E_{sp}^{cl}| = -0.5$. The conditions $0 \leqslant Z_1^{n_1} \leqslant Z$ are fulfilled for the quantum numbers $n_1 = 0$ to $n_1 = 27$. By inspection of the graph, we note that the direct contribution consists of ξ wave functions with quantum numbers in the range $0 \leqslant n_1^{dir} \leqslant 11$, while the indirect contribution spans the $12 \leqslant n_1^{ind} \leqslant 21$ range. Evidently, any possible presence of quasibound Stark states would necessarily correspond to $22 \leqslant n_1^{res} \leqslant 27$ (for $0 < \beta < \beta_c$). Hence, for this particular (E, F, m) set, the maximum number of continua is $n_1^o = 21$ (in accord with the computation of Fig. 2) and, therefore, n_1^o is equal to the maximum number $n_{1,max}^{ind}$ of dark fringes that may be exhibited by the indirect contribution. Furthermore, the direct contribution will exhibit at most $n_{1,max}^{dir} = 11$ dark fringes. Consequently, since $n_{1,max}^{dir} < n_{1,max}^{ind} < n_1^{res}$, the direct contribution will never correspond to resonances. Moreover, because the predicted on-resonance broadening of the image outer ring due to tunneling is strongly connected with the larger values of n_1^{res}, it is expected that this broadening would occur at the outer part of the indirect

contribution. Finally, for $\varepsilon > \varepsilon_{dir} = E_{dir}/|E_{sp}^{cl}| \approx -0.775$ the coexistence of the resonant contribution with the non-resonant direct one would make the uncovering of fringe number changes quite difficult and, additionally, resonant n_1^{res} values around ~ 25 would necessitate the extreme limits of the microscope's spatial resolution. Hence, it is made clear that the most suitable energy range for observing resonant effects is located below E_{dir}, where only the indirect contribution is present and the number of continua and fringes is relatively small.

C. Wave packet propagation calculations

We now turn to a quantitative theoretical description of photoionization microscopy which is based on a wave packet propagation approach, according to which an initial wave function is built at time $t = t_0$ and is subsequently propagated until time $t > t_0$, by solving the TDSE. The main methodological aspects of the approach can be found in [41] and have been modified and adapted for the present purposes in [22]. Using first-order time-dependent perturbation theory the TDSE is (in a.u.),

$$i\frac{\partial \Psi}{\partial t} - (H_{at} + H_F - E)\,\Psi = S(\mathbf{r}, t), \qquad (4)$$

where E is the electron energy, the term $H_F = Fz$ corresponds to the Stark Hamiltonian associated with the static electric field, which is oriented along the z axis, and H_{at} stands for the free-atom Hamiltonian,

$$H_{at} = -\frac{1}{2}\frac{\partial^2}{\partial r^2} + \frac{\hat{L}^2}{2r^2} + V(r) \qquad (5)$$

with $\hat{L}$ the angular momentum operator. In Eq. (5) $V(r)$ is a radial atomic potential describing the interaction between the valence electron and the ionic core. For the hydrogen atom $V(r)$ is simply written as $-1/r$, while for nonhydrogenic atoms with a finite-size ionic core it assumes the following parametric form:

$$V(r) = -\frac{Z_\ell(r)}{r} - \frac{\alpha_d}{2r^4}f(r), \qquad (6)$$

where α_d is the dipole polarizability of the ionic core and $f(r)$ is a cutoff function, remedying the unphysical small-r behavior of the dipole polarization term $-\alpha_d/2r^4$. The effective charge $Z_\ell(r)$ in Eq. (6) is parametrized as $Z_\ell(r) = 1 + (Z-1)e^{-\alpha_\ell^{(1)}r} + \alpha_\ell^{(2)}re^{-\alpha_\ell^{(3)}r}$. For the lithium atom, the nuclear charge is $Z = 3$ and the employed cutoff function as well as all the relevant parameters can be found in [42]. The source term $S(\mathbf{r}, t)$ in Eq. (4) arises from the laser-excited electron wave, assuming the appropriate angular momentum and magnetic quantum numbers ℓ and m, respectively. Specifically, this term is defined as

$$S(\mathbf{r}, t) = f(t)S(r)Y_\ell^m \qquad (7)$$

where Y_ℓ^m is the spherical harmonic of the outgoing electron $[\hat{L}^2 Y_\ell^m = \ell(\ell+1)Y_\ell^m]$ and $S(r)$ is r times the radial 2s function. Finally, in Eq. (7) the employed cw-type time dependence, $f(t) = 1 + \text{erf}(t/t_w)$, gives a smooth turn-on for the laser with time width of t_w, and for larger times the electron wave is continuously launched.

The calculation starts from $t_0 \sim -2t_w$. The wave packet propagation is calculated through the split-operator method [43], on a two-dimensional (r,l) grid. Propagation continues for a time $t > t_0$ for which the transients from the laser turn-on have decayed to zero. The computed wave function is numerically summed over the orbital angular momenta ℓ yielding $\psi_m(\rho,z)$, where m is the azimuthal angular momentum and (ρ,z) denote cylindrical coordinates. For accelerating convergence we apply a Hankel transform to $\psi_m(\rho,z)$ and obtain

$$\Psi_{\mathrm{sim}}(k_\rho,z) = \int d\rho\rho\,\psi_m(\rho,z)J_m(k_\rho\rho), \qquad (8)$$

where $J_m(k_\rho\rho)$ is a Bessel function and k_ρ is proportional to the distance from the z axis at $z = z_{\mathrm{o}}$ (the location of the detector). For $z_{\mathrm{o}} \to -\infty$ the radial distribution is proportional to $k_\rho|\Psi_{\mathrm{sim}}(k_\rho,z_{\mathrm{o}})|^2$. The latter quantity is plotted and compared to the experimental results. The operation of Eq. (8) on the wave function $\psi_m(\rho,z)$ simulates velocity-map imaging [31], since in terms of classical light or particle optics a VMI spectrometer may be regarded as a Fourier (or Hankel for cylindrical symmetry) transformer, relating the particle's radial distribution at the source plane to its vectorial velocity distribution (the latter projected on the detector plane) [32]. In the present case, however, it is employed solely for the purpose of speeding up the calculation, because $\Psi_{\mathrm{sim}}(k_\rho,z_{\mathrm{o}})$ is found to converge much more rapidly than $\psi_m(\rho,z)$. Thus, Eq. (8) effectively propagates the wave function at large distances, without the need to actually solve the TDSE up to these distances.

IV. RESULTS AND DISCUSSION

A. Energy evolution of nonresonant images: General overview

Before presenting the specific resonant features unveiled by the lithium images, it is instructive to discuss first their general evolution with energy. Indeed, resonant signatures may be unveiled only after nonresonant features have been well characterized. Selected images are presented in Figs. 4 and 5(a), for $m = 0$ and $|m| = 1$ final Stark states, respectively. For the employed single-photon excitation scheme from the ground state of Li, both series of images probe the p character of the Stark states. This is evident in the angular distribution exhibited by the $|m| = 1$ set but obscured in the $m = 0$ disk-shaped images, because in the latter case the laser polarization is perpendicular to the PSD plane.

Starting from a "point" image at $\varepsilon \approx -1$ and up to $\varepsilon \approx \varepsilon_{\mathrm{dir}} = E_{\mathrm{dir}}/|E_{sp}^{\mathrm{cl}}|$, we observe, as expected, only the indirect contribution. Although these $\varepsilon < \varepsilon_{\mathrm{dir}}$ *nonresonant* images correspond to a coherent ξ wave function superposition [see Eq. (2)], they show no sign of beating effects and their number of fringes increases smoothly with a rate that can be predicted by inspection of Fig. 2. A few selected radial distributions extracted from the $|m| = 1$ images of Fig. 5(a) are given in Fig. 5(b) along with the corresponding curves obtained by the wave packet calculations. The latter were performed using $F = 1000\,\mathrm{V/cm}$ and $t_w = 50\,\mathrm{ps}$. The wave function was propagated up to 200, 500, or 1000 ps and up to a distance of 1 μm from the origin. For this distance convergence was reached. As may be seen, the computed
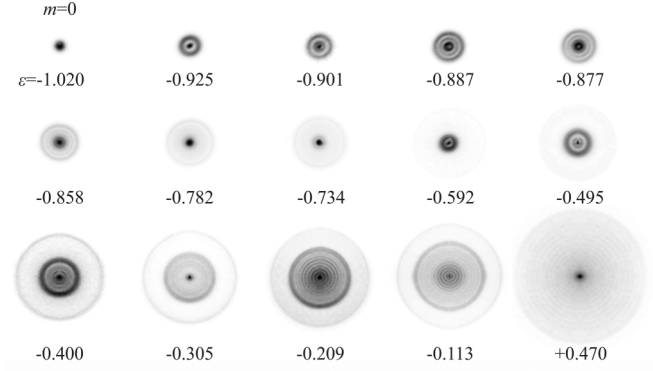

FIG. 4. Energy evolution of $m = 0$ (linear laser polarization parallel to the electric field axis) experimental images for an electric field $F = 1000 \pm 10\,\mathrm{V/cm}$, as estimated by fitting the higher-energy indirect radii to the expression $R_{\mathrm{max}}^{\mathrm{c}}(E) = C[E + |E_{sp}^{\mathrm{cl}}|]^{1/2}$ [39]. The corresponding $\varepsilon = E/|E_{sp}^{\mathrm{cl}}|$ values are indicated below each image. For a number of images near $\varepsilon = \varepsilon_{\mathrm{dir}} \approx -0.775$, the indirect contribution is quite faint and hardly observable. All measurements were performed for an identical number of laser shots. However, the linear grayscale of each image is individually normalized between 100% (black) and 0% (white).
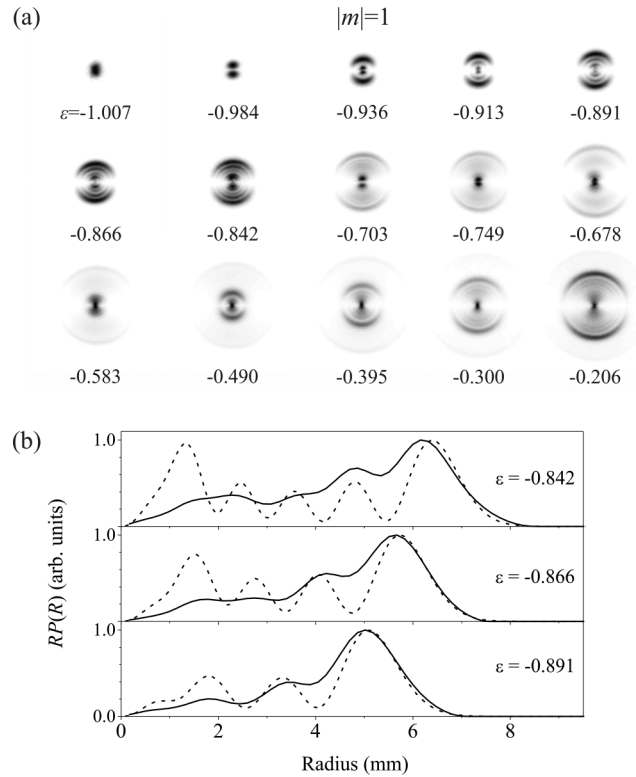

FIG. 5. As in Fig. 4 but for $|m| = 1$ images (linear laser polarization perpendicular to the electric field axis). (a) Recorded images at some selected reduced energies $\varepsilon = E/|E_{sp}^{\mathrm{cl}}|$ for an estimated field of $F = 1000 \pm 10\,\mathrm{V/cm}$. (b) Experimental (continuous line) radial distributions for three selected values of ε, along with the corresponding wave-packet calculations (dashed line) at the above field strength.

nonresonant curves reproduce well the number of fringes, but not equally well their relative intensity and contrast, the latter being of course severely limited by the experimental resolution.

For $\varepsilon \geqslant \varepsilon_{dir}$, the images begin to show the additional direct contribution. Its appearance is accompanied by a considerable (relative) intensity loss of the indirect contribution. The latter is hardly visible just above ε_{dir}, where the spatial size of the direct contribution is quite small. Nevertheless, a small number of central fringes of the indirect contribution are observed within the small region of overlap between the two contributions (see the central part of the $\varepsilon = -0.583$ image of Fig. 5). This is a first manifestation of beating effects between the direct and indirect terms, expected on the basis of the coherent superposition of Eq. (2), and these fringes gain in intensity through interference with the much stronger direct signal. As the energy is increased further, the fringe pattern belonging to the direct contribution develops, which, as expected, is characterized by a relatively small number of well-resolved fringes. The latter become closely spaced and faint at positive energies $\varepsilon > 0$, but they are visible (Fig. 4, $\varepsilon = +0.470$) if the ionization signal is sufficiently strong.

Let us now examine the observed energy dependence of R_{max}^c and R_I. Figure 6 depicts this dependence for an $|m| = 1$ data set, recorded at a slightly different electric field from the one corresponding to the data of Fig. 5. Additionally, the measurements of Fig. 6 are much more closely spaced in the vicinity of E_{sp}^{cl} (steps of $1-2$ cm^{-1}). In fact, the lowest-energy measurement corresponds to the first image where a quantifiable signal could be obtained. For measuring

the two radii, the experimental distribution $p_{expt}(\Theta, R)$ is first angularly integrated and the radial distribution $P_{expt}(R) = \int p_{expt}(\Theta, R) d\Theta$ is obtained. Then, R_{max}^c and R_I are defined here as the outermost inflection points of $R P_{expt}(R)$ for the indirect and direct contributions, respectively. This definition is chosen because these inflection points should lie very close to the classical outer turning points.

The graph of Fig. 6 shows that within the (encircled) low-energy zone, near E_{sp}^{cl}, the behavior of R_{max}^c is irregular, exhibiting a number of oscillations. Using the analytical formula provided in [32] [Eqs. (2a) and 2(b) therein] for the axial voltage variation for our specific VMI geometry, we estimate the field strength at the center between the repeller and extractor electrodes for this data set to be ≈ 998 V/cm. This value corresponds to $E_{sp}^{cl} = -193.4$ cm^{-1}. Fitting of the full data set of Fig. 6 to an expression of the form $R_{max}^c(E) = C[E + |E_{sp}^{cl}|]^{1/2}$ [39] (for $E < 0$ and with $|E_{sp}^{cl}|$ and the scaling factor C as the fitted parameters) leads to $E_{sp}^{cl} = -192 \pm 1$ cm^{-1}. While this value is fairly consistent with the above expectation, the fit leads to a poor reproduction of the behavior of the experimental points. Indeed, the fitted curve (black dashed line in Fig. 6) describes the aforementioned low-energy zone just "on the average" and underestimates the high-energy part of the data by about 2% (somewhat larger than the experimental uncertainty of the radii). In contrast, if the oscillating points below $E \approx -170$ cm^{-1} are excluded, we obtain a quite satisfactory fit for the whole set of data, apart from that oscillating part. On the other hand, the fitted value, $E_{sp}^{cl} = -186 \pm 1$ cm^{-1}, is now found to be considerably lower. A number of reasons may be responsible for the discrepancy. First, as is well known [44], the saddle-point energy is in fact m dependent and given by (in a.u.)

$$E_{sp}(|m|; F) \approx -2F^{1/2}\left[1 - \frac{|m|}{2}F^{1/4} - \frac{3}{32}m^2 F^{1/2}\right]. \quad (9)$$

Using Eq. (9) we find $E_{sp}(|m| = 1; F = 998\text{V/cm}) \approx -189$ cm^{-1}, i.e., the saddle-point energy increases by ≈ 4 cm^{-1} and gets closer to the value extracted from the high-energy fit. The remaining difference may thus arise either from the definitions of R_{max}^c and R_I given above, or from a small overestimation of the field (due, for example, to a laser-atom interaction point displaced by $1-2$ mm from the center between the repeller and extractor electrodes), in conjunction perhaps with a small systematic error in the absolute wavelength calibration of our laser system. Note in passing that, in principle, another estimate for E_{sp}^{cl} may be provided by the indirect radius R_I, the experimental data of which form a quite smooth curve with no irregularities. However, no analytical formula is available for R_I. Therefore, the curve is numerically computed via the expressions given in [39] and it is subsequently scaled in amplitude and energy in order to match the experimental points. This "trial-and-error" procedure leads to $E_{sp}^{cl} = -187 \pm 3$ cm^{-1}, but it is found to be less reliable than the direct fit of R_{max}^c.

The above findings are in complete agreement with the expectations presented in Sec. III B. Specifically, the smooth energy dependence of R_I is compatible with the nonresonant character of the direct contribution. Moreover, the large
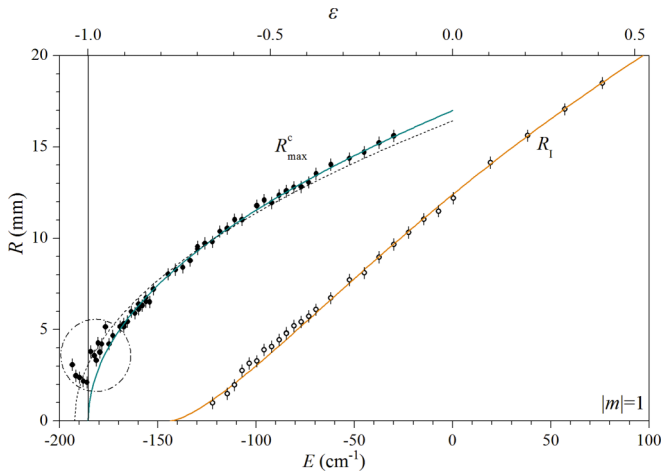

FIG. 6. Experimental maximal radii of the indirect contribution (R_{max}^c, black circles) and of the direct one (R_I, white circles) for an $|m| = 1$ series of images, recorded in the presence of an estimated static field $F = 1000 \pm 10$ V/cm and shown as a function of E and $\varepsilon = E/|E_{sp}^{cl}|$. Encircled are the R_{max}^c data exhibiting a nonclassical behavior which signals electron escape via tunneling. R_{max}^c is fitted to the expression $R_{max}^c(E) = C[E + |E_{sp}^{cl}|]^{1/2}$ [39], by retaining either the full set of data (dashed, black thin line) or the $E \geqslant -170$ cm^{-1} data [continuous, dark cyan (dark gray) heavy line]. The orange (light gray) heavy line curve stands for the numerically computed energy dependence of R_I, which is subsequently matched in amplitude and energy to the experimental points. For the fitted values see the text.
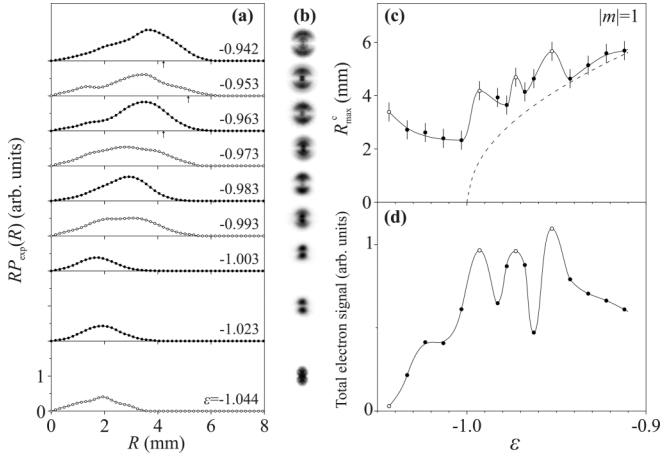
FIG. 7. Experimental radial distributions (a), images (b), outer radii as defined in the text (c), and total integrated electron signal (d), in the vicinity of the saddle-point energy for $|m| = 1$. The quoted values of $\varepsilon = E/|E_{sp}^{cl}|$ are computed using the value $E_{sp}^{cl} = -186 \pm 1$ cm^{-1} determined by a fit to the high-energy points of the $R_{max}^c(E)$ curve of Fig. 6 [dashed line in (c)]. In (a) each experimental distribution is up-shifted proportionally to the energy. Identified resonances are drawn with white circles and, as compared to (c) and (d), some distributions and images are omitted for clarity. The small vertical arrows for the highest three distributions given in (a) denote the corresponding outer radii. In (c) and (d) experimental points are connected with a smooth solid line to guide the eye.

number of fringes of the indirect contribution, along with its signal weakness, makes the experimental search for resonant manifestations in the $\varepsilon > \varepsilon_{dir}$ range quite demanding. In fact, R_{max}^c is usually found to be fairly regular there, signaling the dominance of the continuum n_1 channels over the resonances. On the contrary, by expressing the energy dependence of R_{max}^c and R_I in terms of ε [shown in the upper horizontal axis in Fig. 6 and computed using the E_{sp}^{cl} value extracted from the high energy, $E > -170$ cm^{-1}, fit of $R_{max}^c(E)$], it becomes obvious that a number of images and outer-radius measurements appear to be recorded *below* the saddle-point energy. Furthermore, the irregular (or, better, nonclassical) behavior of the outer radius below and slightly above $\varepsilon \approx -1$ (where the number of continua is small) can be considered as a first potential manifestation of the electron's escape via tunneling and it is fully compatible with the so-called "resonant radius," as defined and discussed by Kondratovich and Ostrovsky [12] (see Fig. 4 therein). This radius is larger than R_{max}^c near E_{sp}^{cl} and it exhibits appreciable magnitude even for $E < E_{sp}^{cl}$. Experimentally, this behavior is observed in both the $|m| = 1$ and $m = 0$ data. In the subsequent sections we present separately these two cases.

B. Resonances: The $|m| = 1$ case

Let us inspect the $|m| = 1$ data first, since they are closer to the hydrogenic case because the relevant wave functions do not contain any $\ell = 0$ core-penetrating component. Specifically, we examine the energy range around $\varepsilon \sim -1$, which is encircled in Fig. 6 and characterized by the aforementioned nonclassical behavior of the outer image radius. Figures 7(a)

and 7(b) show the radial distributions $RP_{expt}(R)$ and the corresponding images, respectively. The evolution of the radius of the outer inflection point as a function of energy is given in Fig. 7(c). Finally, Fig. 7(d) shows the integrated electron signal, proportional to the total excitation cross section. We observe that each sudden increase of the outer radius is accompanied by a cross-section maximum. On the other hand, a comparison between distributions and images reveals that increased outer radii correspond to images exhibiting an external low-intensity "halo" (see images at $\varepsilon = -0.973$ and -0.953; it is not visible in the small lowest-energy image), i.e., a broadened outer image ring, which is a sign of electron tunneling through the η-potential barrier [25]. Therefore, the images with this halo should correspond to resonances. Indeed, despite the low fringe contrast of the images (due to their small size and the microscope's finite spatial resolution) it is fairly evident that, for example, the $\varepsilon = -0.993$ distribution shows an additional fringe ($n_1^{res} = 1$) with respect to the surrounding measurements performed at $\varepsilon = -1.003$ and -0.983 ($n_1^o = 0$). Hence, this image corresponds to the superposition of Eq. (3), where the resonant character dominates or, at least, manifests itself. Therefore, to a good approximation, it is a direct macroscopic projection of a quantum standing wave characterizing the quasibound electronic state ($n_1^{res} = 1$, n_2, $|m| = 1$) with unspecified n_2. Interestingly, there is more than one resonance with the same n_1^{res}. This is the case of the $\varepsilon = -0.973$ and $\varepsilon = -0.953$ distributions, for both of which $n_1^{res} = 2$. Obviously n_2 should differ for these two resonances.

The comparison between theory and experiment proved to be a nontrivial task due to the uncertainty in the knowledge of the exact field strength, as indicated by the different values provided by SIMION calculations, by the predictions based on the analytical axial potential formula given in [32], and by the value extracted from the fit to the high-energy points of the $R_{max}^c(E)$ curve. While the estimations of the field value based on the first two methods differ by $\sim 1\%$, the largest difference with the fit to the image radius amounts to about 6%. With these facts in mind, the present wave packet calculations were performed using a fixed value of $F = 1000$ V/cm, i.e., somewhat different from the 1010 V/cm employed in [23], both being consistent, however, within the estimated accuracy. The calculation was performed using the same parameters employed above for the nonresonant distributions. For the specific choice of F used here, theory revealed several resonant radial distributions and abrupt changes of the number of fringes. Some of these distributions bear similarities with the experimental ones. In particular, the on-resonance broadening of the outer lobe of the distribution is well predicted by the theoretical model for all resonant curves. The energies, however, of the experimental and theoretical resonant distributions differ. Consequently, it was difficult to make a resonance-by-resonance matching. Therefore, we provide in Fig. 8 just an example of a single theoretical resonant radial distribution, along with nonresonant ones lying slightly below and above this resonance. The latter is characterized by $n_1^{res} = 2$ and, consequently, it can be associated with either the $\varepsilon = -0.973$ or the $\varepsilon = -0.953$ experimental resonant distributions. Nevertheless, the shape of the computed resonant curve resembles more the $\varepsilon = -0.953$
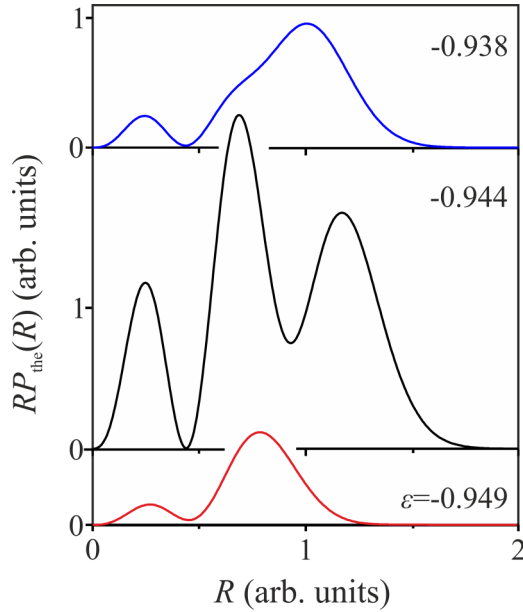
FIG. 8. Theoretically computed distributions, obtained by the wave-packet propagation method for $|m| = 1$ and $F = 1000$ V/cm. The middle resonant ($n_1^{res} = 2, n_2, |m| = 1$) distribution at $\varepsilon = -0.944$ resembles the experimental one recorded at $\varepsilon = -0.953$. For a discussion of the energy difference see the text.
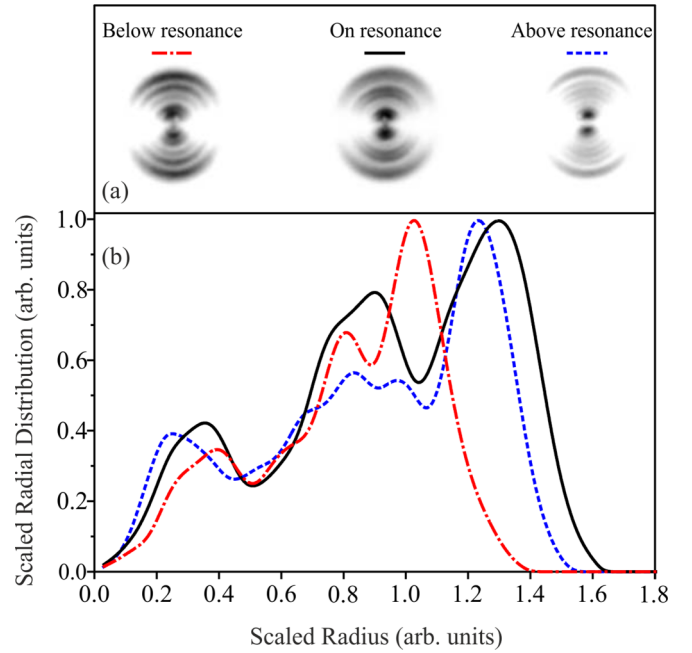

FIG. 9. (a) Measured $|m| = 1$ photoelectron images obtained in the presence of an $F \approx 1000$ V/cm field below a resonance ($\varepsilon \approx -0.815$), on resonance ($\varepsilon \approx -0.789$), and above this resonance ($\varepsilon \approx -0.763$). (b) Radial distributions of the images of (a). The radius (whose size on the detector is ~ 6 mm) is scaled to R_{max}^c [39]. Due to tunneling ionization through the barrier of $V_2(\eta)$, the radius of the resonant image (black continuous curve) is larger than the radii of both nonresonant images, at lower [red (light gray) dash-dotted line] and higher [blue (dark gray) dashed line] photon energies.

experimental one. The contrast of the latter is, here as well, limited by the experimental resolution.

The resonant character is imprinted and evolves over a number of computed distributions across a resonance. This could not be observed experimentally due to the successive recording steps of ~ 1 cm^{-1}, which are rather large for the present purposes. Given also the uncertainty in the field strength, a more comprehensive comparison between theory and experiment is not possible at present. The findings of the He experiment [27] as well as the theoretical work of Ref. [21] could be useful for explaining the observed differences. Both works demonstrated the high sensitivity of resonant manifestations to the value of F. In particular, in Ref. [21], the author showed that, depending on the field strength, an additional bright fringe of the resonant image may either be almost completely merged with the main outer lobe or be clearly visible.

As expected, it becomes much harder to recognize resonant-induced fringe number changes at higher energies (while remaining below ε_{dir}), due to the increased number of open n_1 channels and the decreasing spatial spacing between successive fringes. Therefore, the identification of resonant character at higher energy needs to be based on the appearance of resonance-continuum interference patterns (as implied by Eq. (3)) and the tunneling-induced broadening of the outer ring [23]. Such an example is given in Fig. 9, where an $|m| = 1$ resonant image at $\varepsilon \approx -0.79$ is indeed characterized by a somewhat broader outer ring as compared to the red and blue off-resonance images. Moreover, the resonant image exhibits a pronounced beating pattern while the off-resonance ones show a fairly smooth fringe intensity variation.

C. Resonances: The $m = 0$ case

Apart from the laser polarization, the $m = 0$ data were recorded under supposedly the same experimental conditions and field strength as the $|m| = 1$ ones. As opposed, however, to the latter case, we were able to unambiguously assign the resonant character to just a single image. Figure 10 shows the relevant radial distributions, images, outer inflection point radii, and total electron signal in the vicinity of this resonance. Despite the low fringe contrast, the resonant radial distribution at $\varepsilon = -0.975$ [Fig. 9(a)] clearly exhibits an intense central lobe and, consequently, an additional dark fringe with respect to the nonresonant distributions having a single dark fringe ($n_1^o = 1$). Therefore it can be characterized by the ($n_1^{res} = 2, n_2, m = 0$) set of quantum numbers. The halo at large radius [Fig. 10(b)], stemming from the tunneling effect, is also apparent here and is responsible for the observed increase of the maximum image radius by about 30%. This is evident in Fig. 10(c) where the measured outer radii are compared to the classical $R_{max}^c(E)$ curve, fitted to the high-energy points of this set. The fit showed that a few images were again recorded below the value of E_{sp}^{cl} extracted from the fit. Apart from their nonclassical outer radii, however, these images showed no other sign of resonant character. Note finally that the strong maximum of the total electron signal shown in Fig. 9(d) at $\varepsilon \approx -0.945$ coincides with a weak local maximum of the outer image radius [see Fig. 10(c)], but there is no apparent fringe number change in the corresponding image (not shown).
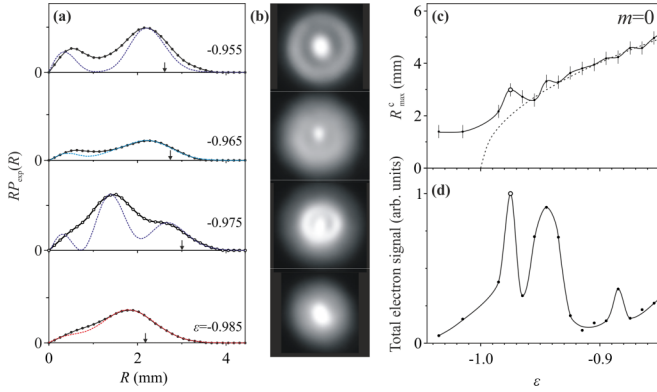
FIG. 10. As in Fig. 7 but for $m = 0$. The quoted values of $\varepsilon = E/|E_{sp}^{cl}|$ are computed using the value $E_{sp}^{cl} = 187 \pm 1 \, \mathrm{cm}^{-1}$, determined by a fit to the high-energy points of the corresponding $R_{max}^c(E)$ curve [dashed line in (c)]. Data drawn with white open circles denote the identified resonance. Theoretically computed distributions, obtained by the wave-packet propagation method, are drawn in (a) with dashed lines. All theoretical curves are redshifted in energy by $\Delta\varepsilon \approx 0.03$, and each curve was appropriately scaled in amplitude in order to match the corresponding experimental maximum. In (c) and (d) experimental points are connected with a smooth solid line to guide the eye.

Furthermore, for the weak total electron signal maximum at $\varepsilon \approx -0.88$ seen in Fig. 9(d), neither the image nor its outer inflection point radius is affected. This behavior may stem from the very low fringe contrast or from the employed field strength, upon which, as mentioned above, the appearance of the resonant image critically depends [21]. Another possible explanation, however, may involve the larger core penetration exhibited by the $m = 0$ states as compared to the $|m| = 1$ ones. That is, while for non-core-penetrating states a manifestation of the resonant character in the images and their outer radii is always accompanied by a maximum in the total electron signal, the reverse is not always true for core-penetrating states. This is a noticeable difference between the $|m| = 1$ and $m = 0$ data, as revealed by the comparison between Figs. 7 and 10. Nevertheless, the very fact that core-penetrating quasibound states may, under certain conditions, manifest themselves in wave-function imaging is quite encouraging.

Wave packet calculations for $m = 0$ were also performed at a fixed value of $F = 1000 \, \mathrm{V/cm}$ and in the energy range shown in Fig. 10. Although the search for distributions showing resonant effects was not exhaustive, just two resonant distributions were found, one of them with $n_1^{res} = 2$. However, the location of this $n_1^{res} = 2$ distribution differs by about $\Delta\varepsilon = 0.03 \, (\approx 6 \, \mathrm{cm}^{-1})$ from the experimental one. By redshifting all computed (resonant and nonresonant) distributions by this energy difference we obtain a fairly satisfactory agreement with the experiment [see Fig. 10(a)], particularly if we take into account the finite spatial resolution of the detector.

V. SYNOPSIS AND OUTLOOK

We have presented a photoionization microscopy study on the lithium atom, which, along with the by now well-known

nonresonant effects, revealed signatures of quasibound states on the obtained images. The recording of the projections of quasidiscrete electronic states (n_1, n_2, m) constitutes the realization of a wave-function microscopy experiment proposed about 30 years ago [11,12]. The most persistent resonant manifestation was found to be the nonclassical evolution of the image radius related to the on-resonance broadening of the outer image ring [12,19,25]. The latter is associated with electron tunneling through the barrier of $V_2(\eta)$ and carries information on its presence near the ionic core. Indeed, almost every classically unexpected behavior of the outer image radius discovered in the present work may be associated with a resonance. On the other hand, although on-resonance changes of the number of dark fringes have been also observed, the quasibound states did not dominate the interference patterns, at least not to the degree that it was theoretically predicted [12] and experimentally observed [24] in the hydrogen atom. This lower resonant fringe contrast with respect to the hydrogenic case is essentially attributed to the presence of the nonhydrogenic Li^+ ionic core. The core scatters a fraction of the resonant flux to continuum electron waves and modifies the weights of each wave in the coherent sum related to the recorded image in favor of these continuum waves. Nevertheless, a portion of the resonant flux survives and the resonant contribution to the recorded images appears to be "superimposed" on the continuum contribution, the latter being always present. The experience gained so far on small atoms like Li and He [27] could guide the design of experiments where these atoms could be photoionized under more complex conditions, for example, under the simultaneous presence of electric and magnetic fields [45].

Both experimental data and theoretical calculations based on the wave-packet propagation approach showed the existence of resonances exhibiting the above-mentioned specific characteristics. A fully quantitative comparison between theory and experiment was, however, hindered mainly by a poor knowledge of the field strength. For the latter, a level of relative precision far better than $\sim 1\%$ is evidently required. On the other hand, matching quantitatively theoretical and experimental resonant and nonresonant radial distributions may offer the opportunity in the future to determine the field strength with much higher precision, comparable perhaps to that of other proposed methodologies [46]. To this end, it would probably be preferable to employ different, time-independent, and less time-consuming theoretical approaches, capable of predicting resonant images in nonhydrogenic atoms such as the alkali-metal atoms [20,22,28] and xenon [19]. Nevertheless, the wave packet propagation approach is highly valuable in connection with foreseeable time-resolved experiments aimed at an investigation of tunneling ionization dynamics and the corresponding buildup of the squared modulus of the wave function.

Finally, it seems that it is now the time to envision possible extensions of photoionization microscopy, for obtaining information on the wave function's phase, apart from its modulus. For this purpose, the technique will probably have to incorporate weak-measurement concepts [6,7], employed so far solely for photons [8] but not yet for massive particles and atomic systems. This type of measurement would evidently require modifications of the photoionization microscope

design, and, most probably, time-dependent information as well as novel theoretical developments. Therefore, we may anticipate with enough confidence that, despite the fact that photoionization microscopy is already $\sim$15 years old, the topic is still in its infancy, and more fruitful advances are yet to come.

[1] J. Repp, G. Meyer, S. M. Stojkovic, A. Gourdon, and C. Joachim, Phys. Rev. Lett. **94**, 026803 (2005).

[2] P. Puschnig, S. Berkedile, A. J. Flemming, G. Koller, K. Emtsev, T. Seyller, J. D. Riley, C. Ambrosch-Draxl, F. P. Netzer, and M. Ramsey, Science **326**, 702 (2009).

[3] M. Feng, J. Zhao, and H. Petek, Science **320**, 359 (2008).

[4] D. Shafir, Y. Mairesse, D. M. Villeneuve, P. B. Corkum, and N. Dudovich, Nat. Phys. **5**, 412 (2009).

[5] J. Itatani, J. Levesque, D. Zeidler, H. Niikura, H. Pépin, J. C. Kieffer, P. B. Corkum, and D. M. Villeneuve, Nature (London) **432**, 867 (2004).

[6] Y. Aharonov, D. Z. Albert, and L. Vaidman, Phys. Rev. Lett. **60**, 1351 (1988).

[7] S. Kocsis, B. Braverman, S. Ravets, M. J. Stevens, R. P. Mirin, L. K. Shalm, and A. M. Steinberg, Science **332**, 1170 (2011).

[8] J. S. Lundeen, B. Sutherland, A. Patel, C. Stewart, and C. Bamber, Nature (London) **474**, 188 (2011).

[9] I. I. Fabrikant, Zh. Eksp. Teor. Fiz. **79**, 2070 (1980) [JETP **52**, 1045 (1980)].

[10] Yu. N. Demkov, V. D. Kondratovich, and V. N. Ostrovsky, Pis'ma Zh. Eksp. Teor. Fiz. **34**, 425 (1981) [JETP Lett. **34**, 403 (1981)].

[11] V. D. Kondratovich and V. N. Ostrovsky, J. Phys. B **17**, 1981 (1984); **17**, 2011 (1984); **23**, 21 (1990).

[12] V. D. Kondratovich and V. N. Ostrovsky, J. Phys. B **23**, 3785 (1990).

[13] C. Blondel, C. Delsart, and F. Dulieu, Phys. Rev. Lett. **77**, 3755 (1996).

[14] A. J. R. Heck and D. W. Chandler, Annu. Rev. Phys. Chem. **46**, 335 (1995); C. Bordas, F. Paulig, H. Helm, and D. L. Huestis, Rev. Sci. Instrum. **67**, 2257 (1996).

[15] C. Blondel, W. Chaibi, C. Delsart, C. Drag, F. Goldfarb, and S. Kröger, Eur. J. Phys. D **33**, 335 (2005); F. Goldfarb, C. Drag, W. Chaibi, S. Kröger, C. Blondel, and C. Delsart, J. Chem. Phys. **122**, 014308 (2005).

[16] C. Nicole, H. L. Offerhaus, M. J. J. Vrakking, F. Lépine, and C. Bordas, Phys. Rev. Lett. **88**, 133001 (2002).

[17] C. Bordas, F. Lépine, C. Nicole, and M. J. J. Vrakking, Phys. Rev. A **68**, 012709 (2003).

[18] F. Lépine, C. Bordas, C. Nicole, and M. J. J. Vrakking, Phys. Rev. A **70**, 033417 (2004).

[19] F. Texier, Phys. Rev. A **71**, 013403 (2005).

[20] L. B. Zhao, I. I. Fabrikant, M. L. Du, and C. Bordas, Phys. Rev. A **86**, 053413 (2012).

[21] L. B. Zhao, EPL **109**, 23002 (2015).

[22] P. Giannakeas, F. Robicheaux, and C. H. Greene, Phys. Rev. A **91**, 043424 (2015).

[23] S. Cohen, M. M. Harb, A. Ollagnier, F. Robicheaux, M. J. J. Vrakking, T. Barillot, F. Lépine, and C. Bordas, Phys. Rev. Lett. **110**, 183001 (2013).

[24] A. S. Stodolna, A. Rouzée, F. Lépine, S. Cohen, F. Robicheaux, A. Gijsbertsen, J. H. Jungmann, C. Bordas, and M. J. J. Vrakking, Phys. Rev. Lett. **110**, 213001 (2013).

[25] L. B. Zhao and J. B. Delos, Phys. Rev. A **81**, 053417 (2010); **81**, 053418 (2010).

[26] L. B. Zhao, D. H. Xiao, and I. I. Fabrikant, Phys. Rev. A **91**, 043405 (2015).

[27] A. S. Stodolna, F. Lépine, T. Bergeman, F. Robicheaux, A. Gijsbertsen, J. H. Jungmann, C. Bordas, and M. J. J. Vrakking, Phys. Rev. Lett. **113**, 103002 (2014).

[28] L. B. Zhao, I. I. Fabrikant, J. B. Delos, F. Lépine, S. Cohen, and C. Bordas, Phys. Rev. A **85**, 053421 (2012).

[29] D. A. Harmin, Phys. Rev. A **24**, 2491 (1981); **26**, 2656 (1982).

[30] F. Lépine, S. Zamith, A. de Snaijer, C. Bordas, and M. J. J. Vrakking, Phys. Rev. Lett. **93**, 233003 (2004).

[31] A. T. J. B. Eppink and D. H. Parker, Rev. Sci. Instrum. **68**, 3477 (1997).

[32] M. M. Harb, S. Cohen, E. Papalazarou, F. Lépine, and C. Bordas, Rev. Sci. Instrum. **81**, 125111 (2010).

[33] H. L. Offerhaus, C. Nicole, F. Lépine, C. Bordas, F. Rosca-Pruna, and M. J. J. Vrakking, Rev. Sci. Instrum. **72**, 3245 (2001).

[34] B. Baguenard, J. B. Wills, F. Pagliarulo, F. Lépine, B. Climen, M. Barbaire, C. Clavier, M. A. Lebeault, and C. Bordas, Rev. Sci. Instrum. **75**, 324 (2004).

[35] H. A. Bethe and E. E. Salpeter, *Quantum Mechanics of One and Two-Electron Atoms* (Springer, Berlin, 1957).

[36] K. Reid, Annu. Rev. Phys. Chem. **54**, 397 (2003).

[37] Y. Ralchenko, A. Kramida, J. Reader, and NIST ASD Team, 2011 NIST Atomic Spectra Database (version 4.1), http://physics.nist.gov/asd.

[38] T. F. Gallagher, *Rydberg Atoms* (Cambridge University Press, Cambridge, 1994).

[39] C. Bordas, Phys. Rev. A **58**, 400 (1998).

[40] C. Nicole, I. Sluimer, F. Rosca-Pruna, M. Warntjes, M. J. J. Vrakking, C. Bordas, F. Texier, and F. Robicheaux, Phys. Rev. Lett. **85**, 4024 (2000).

[41] T. Topcu and F. Robicheaux, J. Phys. B **40**, 1925 (2007).

[42] M. Aymar, S. Feneuille, and M. Klapisch, Nucl. Instrum. Methods **90**, 137 (1970).

[43] F. Robicheaux and J. Shaw, Phys. Rev. Lett. **77**, 4154 (1996); Phys. Rev. A **56**, 278 (1997).

[44] W. E. Cooke and T. F Gallagher, Phys. Rev. A **17**, 1226 (1978); M. G. Littman, M. M. Kash, and D. Kleppner, Phys. Rev. Lett. **41**, 103 (1978).

[45] L. Wang, H. F. Yang, X. J. Liu, H. P. Liu, M. S. Zhan, and J. B. Delos, Phys. Rev. A **82**, 022514 (2010).

[46] G. D. Stevens, C. H. Iu, T. Bergeman, H. J. Metcalf, I. Seipp, K. T. Taylor, and D. Delande, Phys. Rev. A **53**, 1349 (1996).